Bulgarian Journal of Physics vol. **XX** (20XX) 1–16

The Study of Temperature Dependent Structural and Elastic Properties of $Ni_{0.5}Zn_{0.5}Gd_{0.05}Fe_{1.95}O_4$ Ferrite Nanoparticles

K. Vijaya Kumar[*1], **S.D. Bhavani**[2], **M.A. Shukur**[1,3]

[1]Department of Physics, JNTUH College of Engineering Sultanpur, Sultanpur, Pulkal (M), Sangareddy-District, 502273, TS, India
[2]Department of Chemistry, Govt. Degree College Zaheerabad, 502220, TS, India
[3]Department of Physics, SRR Govt. Arts & Science College, Karimnagar, 505001, TS, India
[*]Corresponding author E-mail: kvkphd@gmail.com; kvkumar@jntuh.ac.in

Received *23 August 2021*, Revised *09 November 2021*

Abstract. The ferrite nanoparticles of composition $Ni_{0.5}Zn_{0.5}Gd_{0.05}Fe_{1.95}O_4$ were prepared by sol-gel method. In order to study the temperature dependent structural and elastic properties, the prepared powder was divided into five parts. The first part was considered as the as-prepared sample and the remaining four parts were calcinated at temperatures 600, 700, 800 and 900°C. The X-ray diffraction patterns confirmed the formation of cubic spinel structure in single phase and Fd3m space group without any impurity peaks. The crystallite size was found 17.61 nm in case of as-prepared sample whereas it was increased from 11.75 nm to 18.13 nm with the increment of calcination temperature from 600 to 900°C. The lattice parameter was found maximum, 8.389 Å in case of as-prepared sample whereas it was found decreased to 8.360 Å with the increment of calcination temperature. From the FE-SEM micrographs, the average grain size was found 100.2 nm in case of as-prepared sample whereas it was found increased to 152.3 nm with the increment of calcination temperature. The FTIR spectroscopy showed six absorption peaks in the range 350 to 3450 cm^{-1}. The first two absorption bands were found in the ranges 360–448 cm^{-1} and 553–575 cm^{-1} which attributes the presence of spinel structure. The study of elastic properties was made by measuring the longitudinal velocity (V_l) and shear velocity (V_s) which were carried out at room temperature using pulse transmission technique at the frequency of 1 MHz. The elastic moduli were found increased with the calcination temperature whereas zero porous moduli were found decreased with the calcination temperature.

KEY WORDS: XRD, SEM, FT-IR, Elastic Moduli.

1 Introduction

The general formula of spinels structures is AB_2O_4, where A is a divalent transition metal ion (Ni, Zn, Cd, Co, Cu, etc.) and B is a trivalent metal ion (Fe, Al & Fe, Cr & Fe, Gd & Fe, etc.). Over the former several decades, the spinel structures have fascinated great attention by the researchers due to their enormous applications along with their good biocompatibility, low toxicity and their magnetism [1, 2]. These kind materials are presently considered among the most successful magnetic nanoparticles for technological and medical applications such as magnetocaloric refrigerators, magnetic memory, solar water oxidation, electrochemical supercapacitor applications, biological applications, lithium-ion batteries, contrast enhancement in magnetic resonance imaging (MRI) and magnetic fluid hyperthermia [3–10]. Therefore, an understanding of the structural, electrical, magnetic and elastic properties of these spinels is acquired great importance from both basic and applied researchers. These properties can be altered by synthesis methods, calcination temperature and by doping suitable elements into the A-site or/and B-site. Particularly, the spinel ferrites have a face-cantered cubic (fcc) structure, which consists of a cubic close-packed oxygen lattice. The unit cell of a spinel ferrite consists of 16 trivalent iron ions, 8 divalent metal ions and 32 oxygen ions. The spinel structure contains two interstitial sites, occupied by metal cations with octahedral (B) and tetrahedral (A) oxygen coordination. In general, the cationic distribution between the two sites is quantified by the inversion degree (γ), which is defined as the fraction of divalent ions in the octahedral sites. In the normal spinel configuration, the Fe^{3+} ions (16) occupy the octahedral sites, while the divalent M^{2+} ions (8) occupy the tetrahedral sites, giving the empirical formula $(M^{2+})^{A}[Fe^{3+}]^{B}O_4$. On the other hand, in the inverse spinel configuration, half of the Fe^{3+} ions (8) occupy the tetrahedral sites, while the other half of Fe^{3+} ions (8) and the M^{2+} ions (8) occupy the octahedral sites, yielding the empirical formula $(Fe^{3+})^{A}[M^{2+}Fe^{3+}]^{B}O_4$. The structure in some cases can also be mixed or random spinel also. However, super exchange interactions between magnetic ions located in the same kind of interstitial sites (J_{A-A} and J_{B-B}) lead to two ferromagnetically ordered sub-lattices. In the case of nanoparticles, the larger surface area creates surface relaxation, surface bond bending, surface effect and consequently spins canting which modifies the contribution of each interaction. The relation between structures and physical properties for ferrite nanoparticles require a careful consideration. Therefore, various methods, including, forced hydrolysis in polyol, ball milling, coprecipitation, sol-gel auto-combustion and hydrothermal/solvothermal method, etc. [3, 11–14], have extensively been used to synthesize spinel ferrite nanoparticles with different sizes and shapes. Ball milling method is favourable to produce a highly crystalline nanostructures, but always leads to agglomeration in high reaction temperature and long time. In contrast, sol-gel method is preferred to synthesize nanoparticle due to its better control over the shape and size at lower temperatures. This method requires

short process time and can produce large quantity with remarkable purity at low cost [15]. The mixed Ni-Zn ferrite is a member of the class of the spinel ferrites which is widely advertised for its applications in magnetic, magneto-optical and magneto-dielectric devices. Under normal conditions, spinel Ni-Zn ferrite is a typical ferrimagnetic material possessing mixed spinel structure $(Fe_i^{3+}M_{1-i}^{2+})[M_i^{2+}Fe_{2-i}^{3+}]O_4$ [16, 17], where i is the inversion degree, ( ) and [ ] represent tetrahedral and octahedral positions respectively, which belongs to Fd3m space group. The cation arrangement can vary between two extreme cases. One of them is the normal spinel ($i = 0$), where all the divalent elements occupy tetrahedral A sites and all the trivalent elements occupy octahedral B sites. The other one is the inverse spinel ($i = 1$), where all the divalent elements occupy octahedral B sites and all trivalent elements are equally distributed between tetrahedral (A) sites and octahedral (B) sites. The third one is random spinel with the cation distribution in the way of intermediate between normal and inverse spinel ($i.e.$, partially inverse spinels; $0 < i < 1$) are also very frequent [18]. Furthermore, Ni-Zn ferrites are characterized by high surface area, chemical stability, high saturation magnetization, high Curie temperature, low coercivity (soft magnetic), high permeability, high dielectric constant, low losses, semiconductor dielectric transition and they can find wide application in the high frequency region of electronic devices [19]. On substitution of Zn^{2+} in Ni ferrite the Fe^{3+} ions migrate from (A) to [B] site and consequently the Fe_A-O-Fe_B interaction becomes weak. Few studies have reported that the magnetic and electrical properties can be changed and tuned by gadolinium doping in Ni-Zn ferrites [20, 21]. The introduction of Gd^{3+} ions leads to significant variations of cation distribution over the A and B sites depending on the method of synthesis and Gd concentration [21]. For nanometric Ni-Zn ferrites, it is possible to obtain good magnetic properties and high performance at relatively low sintering temperature. Also, the magnetic properties of Ni-Zn ferrite nanocrystals depend on different sizes, shapes, and synthesis methods. Beji et al. [11] prepared a series of polyol-made Ni-Zn ferrite nanoparticles with varying annealing temperatures to optimize the structural and magnetic properties and found that calcinating at different temperatures ranged from 400 to 800°C provides changes of the magnetic properties of these particles. In case of Lahouli et al. [23], the investigation of dielectric properties of $Ni_{0.6}Zn_{0.4}Fe_{1.5}Al_{0.5}O_4$ ferrite nanoparticles annealed at 600, 900, and 1200°C was done and found that the dielectric properties of the system improved on increasing the temperature. Further, K.V. Kumar and D. Ravinder et al. [20, 21] have studied effect of gadolinium substitution on electrical and dielectric properties of Ni-Zn ferrites. Likewise, several people have investigated temperature dependent magnetic and dielectric properties. But, there is no study found in the literature on calcination temperature dependent structural and elastic properties of ferrite nanoparticles. Therefore, we have taken up the study of calcination temperature dependent structural and elastic properties of $Ni_{0.5}Zn_{0.5}Gd_{0.05}Fe_{1.95}O_4$ nanoparticles prepared by sol-gel method.

2 Experimental

The composition of $Ni_{0.5}Zn_{0.5}Gd_{0.05}Fe_{1.95}O_4$ spinel ferrite nanoparticles were prepared by sol-gel method [24]. The starting materials such as nickel nitrate, zinc nitrate, iron nitrate, gadolinium nitrate, citric acid and ammonia of analytical grade were used. The solution of nickel nitrate ($Ni(NO_3)_2{\cdot}6H_2O$), ferric nitrate ($Fe(NO_3)_3{\cdot}9H_2O$), zinc nitrate ($Zn(NO_3)_2{\cdot}6H_2O$) and gadolinium nitrate ($Gd(NO_3)_3$) in their stoichiometry were dissolved in a de ionized water. Citric acid was then added to the prepared aqueous solution to chelate Ni^{2+}, Zn^{2+}, Gd^{3+} and Fe^{3+} in the solution. The molar ratio of citric acid to total moles of nitrate ions was adjusted at 1:3 ratio. The mixed solution was neutralized to the pH value 7 by adding ammonia (NH_3) solution in adequate proportion. The neutralized solution was evaporated to dry by heating at about 100°C on a hot plate with continuous stirring, until it becomes viscous and finally formed a viscous gel. Increasing the temperature up to about 300°C lead to ignite the formed gel, then the dried gel burnt completely in a self-propagating combustion manner to form a loose powder [25, 26]. The prepared powder was divided into five parts, one part was not calcinated and just it was treated as as-prepared sample and the remaining four parts were calcinated at 600, 700, 800 & 900°C for 8 h followed by sintering at 1300°C for 4 h in air.

The structural characterization was carried out by powder X-ray diffraction (XRD) using Phillips expert diffractometer at room temperature in the 2θ range of 20–80°. The bulk densities of all the samples were calculated by means of immersion method. With the help of these bulk densities and X-ray densities, the porosity values were calculated. Micro structural studies of the samples were carried out using a field emission scanning electron microscope (FE-SEM) (Apreo LoVac, Make: FEI). Fourier transform infrared spectroscopy (FTIR) was recorded on a Jasco FTIR spectrometer (Model: FT/IR4200typeA) within a range of 400–4000 cm^{-1}. The longitudinal and shear wave velocities were calculated by ultrasonic pulse transmission technique using a pulse generator RPR-4000 (RITEC INC., USA). The pulse oscillator generated RF pulses and a transmitting transducer converted them into acoustic pulses. The acoustic pulses propagating through the disc shaped testing sample of thickness ~ 2.5 mm and diameter $\sim$ 10 mm, these pulses were converted into electrical signals at the receiving transducer. The amplified output signals were displayed on a storage oscilloscope. Quartz transducers with ability to generate ultrasonic signals of 1 MHz were used for the both the operations like generating and detecting signal. The longitudinal and shear wave signals were generated by using X and Y-cut transducers respectively. The transmission time of the ultra sound was measured up to an accuracy of 1 μs using a 100 MHz digital storage oscilloscope (Tektronix model: TDS2012C). The overall correctness of these measurements in velocity was about 0.25% and elastic moduli were about 0.5%. The block diagram of ultrasonic pulse transmission technique is shown in Figure 1.

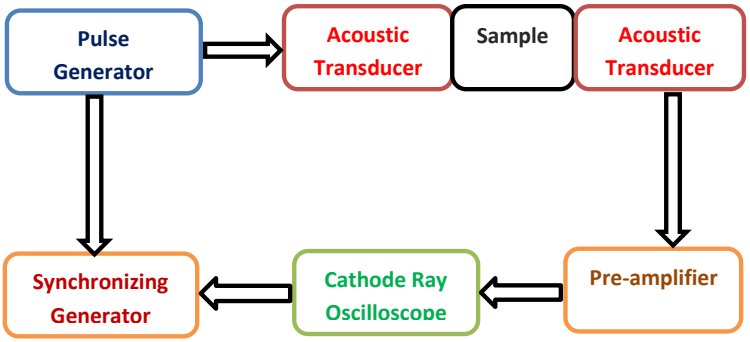

Figure 1. Block diagram of pulse transmission technique

3 Results and Discussions

3.1 X-ray diffraction

The X-ray diffraction patterns of all the samples are shown in Figure 2. A systematic investigation of the XRD data evidently reveals that all the samples are having single phase without any noticeable impurity. Rietveld refinement technique [27] was used to analyze the XRD data by assuming spinel cubic structure and Fd3m space group. The Rietveld refinement is fitted for the sample calcinated at 900°C and is shown in Figure 2 (Top). The calculated values such as lattice parameter, crystallite size, X-ray density, bulk density and porosity percentage of all the samples are furnished in Table 1. As per the earlier reports,

Table 1. Lattice parameters, crystallite size and average grain size of $Ni_{0.5}Zn_{0.5}Gd_{0.05}Fe_{1.95}O_4$ ferrite nanoparticles (as-prepared and calcinated at 600, 700, 800 & 900°C)

		Calcination temperature (°C)			
Parameter	As-prepared	600	700	800	900
a (Å)	8.389(1)	8.382(2)	8.373(1)	8.367(1)	8.360(3)
b (Å)	8.389(1)	8.382(2)	8.373(1)	8.367(1)	8.360(3)
c (Å)	8.389(1)	8.382(2)	8.373(1)	8.367(1)	8.360(3)
V (Å^3)	590.3785	588.9019	587.0070	585.7459	584.2770
R_P (%)	2.173	2.256	2.356	2.228	2.210
R_{WP} (%)	3.352	3.421	3.395	3.428	3.302
R_{EXP} (%)	3.220	3.227	3.086	3.265	3.145
Goodness of fit (S)	1.04	1.06	1.10	1.05	1.05
Crystalline size (nm)	17.61	11.75	12.98	14.44	18.13
Avg. Grain size (nm)	100.2	117.22	132.23	146.50	152.30

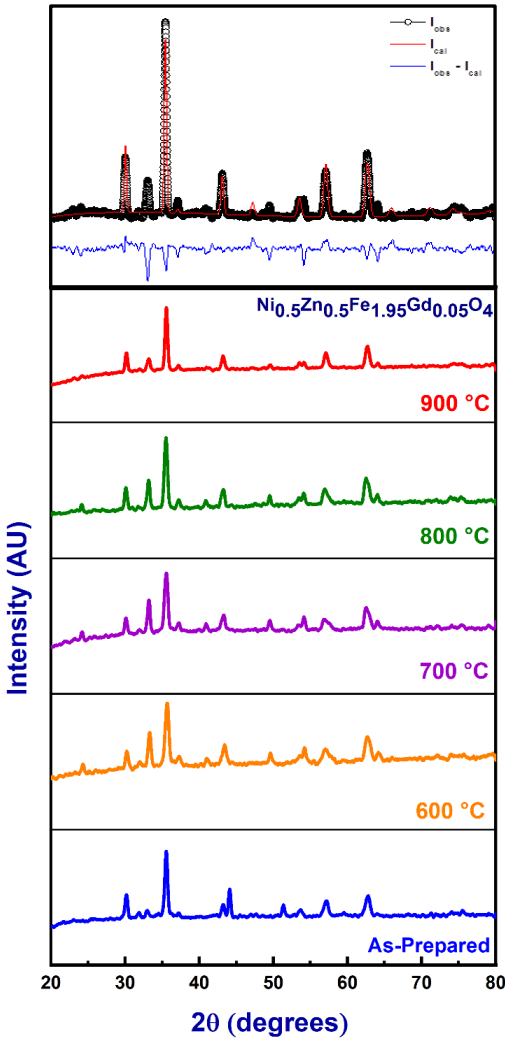

Figure 2. X-ray diffraction patterns of $Ni_{0.5}Zn_{0.5}Gd_{0.05}Fe_{1.95}O_4$ ferrite nanoparticles (as-prepared and calcinated at 600, 700, 800 & 900°C).

a systematic variation of properties with divalent, trivalent and tetravalent metal ions doped into ferrites have been reported [28–36], but the study of properties of gadolinium ferrites with calcinated temperature is not reported. Huixue Yao et al showed that the crystallite size is shrinking with the increasing doping content of Gd^{3+} ions [37]. They tried to clarify the reason for this decreasing trend. On the one hand, the large size mismatching between Gd^{3+} and Fe^{3+} can lead to grain anisotropy when the replacement of ions generates strain inside crys-

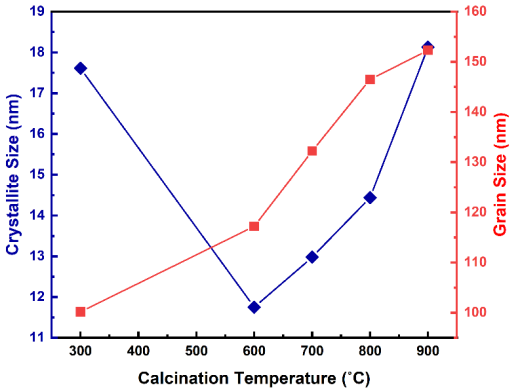

Figure 3. Variation of crystallite size and average grain size of $Ni_{0.5}Zn_{0.5}Gd_{0.05}Fe_{1.95}O_4$ ferrite nanoparticles with calcination temperature (as-prepared and calcinated at 600, 700, 800 & 900°C).

tal volume with an increase of Gd^{3+} doping content. Moreover, the balance of the crystal anisotropy and volume strain to each other can maintain in a stable equilibrium state. As a result, the grain size decreases with an increase in Gd^{3+} substitution contents for decrease of the volume strain. On the other hand, the Fe^{3+} takes up either tetrahedral or octahedral sites, whereas Gd^{3+} ions tend to occupy the octahedral site in the crystal structure of $NiFe_{2-x}Gd_xO_4$. The Gd^{3+} ions enter the lattice owing to the other strain being from segmental gadolinium ions, prohibiting the crystallization of $NiFe_2O_4$. In the present study, the crystallite size was found 17.61 nm in case of as-prepared sample whereas the crystallite size was increased gradually from 11.75 nm to 18.13 nm with the increment of calcination temperature from 600 to 900°C as shown in Figure 3. The lattice parameter was found maximum (8.389 Å) for as-prepared sample and it was found decreased to 8.360 Å with the increment of calcination temperature. The decrement of lattice parameter can be attributed to the occupation of Gd^{3+} ions in octahedral voids, instead of tetrahedral lattice sites in a gadolinium doped Ni-Zn ferrite nanoparticle [37].

3.2 Field emission scanning electron microscopy

The micro structural investigation of all the samples was carried out using a Field Emission Scanning Electron Microscope (FE-SEM) and the micrographs of all the samples are shown in Figure 4. It can be observed that the shape of the grains was not having any particular pattern in case of all the samples [38–40]. From the FE-SEM micrographs, the average grain size was found 100.2 nm for as-prepared sample and it was found increased gradually to 152.3 nm with the calcination temperature as shown in Figure 3. The average grain size of all the samples are furnished in Table 1.

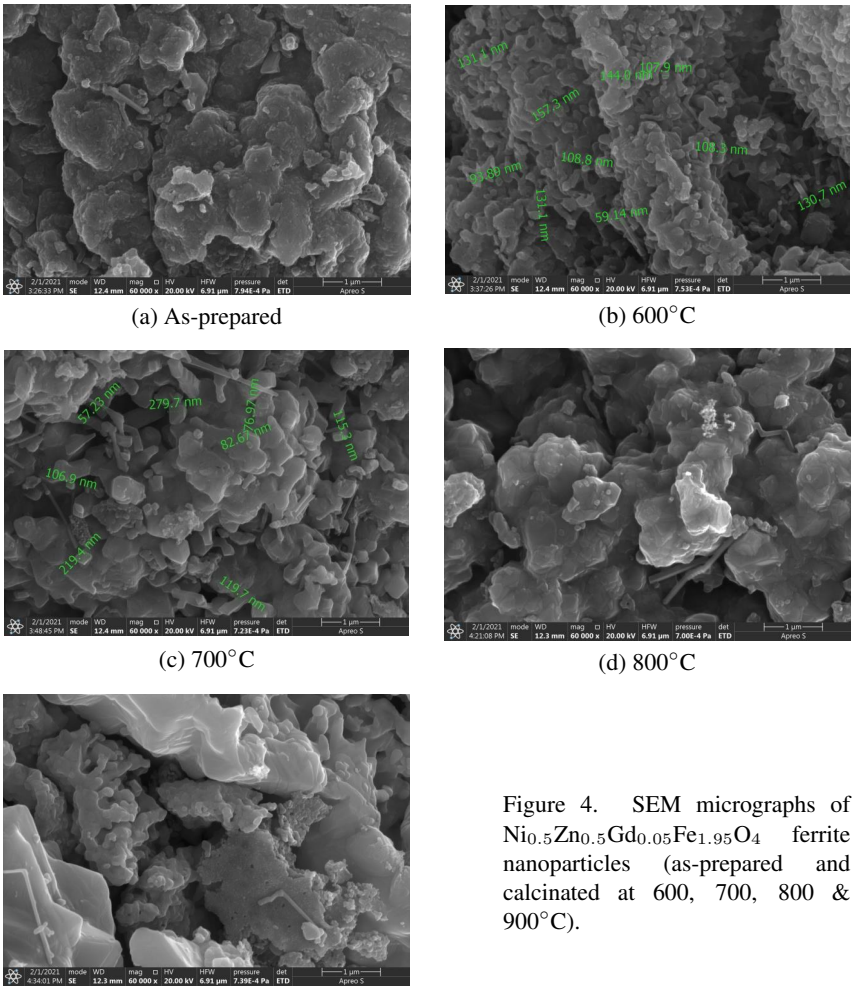

(a) As-prepared

(b) 600°C

(c) 700°C

(d) 800°C

(e) 900°C

Figure 4. SEM micrographs of $Ni_{0.5}Zn_{0.5}Gd_{0.05}Fe_{1.95}O_4$ ferrite nanoparticles (as-prepared and calcinated at 600, 700, 800 & 900°C).

3.3 FTIR spectra

The FTIR transmission spectra of all the samples are shown in Figure 5. The six characteristic absorption bands for all the samples are furnished in Table 2. The first two absorption bands were found in the ranges 360–448 cm^{-1} and 553–575 cm^{-1} which corresponds to stretching vibration of the metal-oxygen bond in octahedral sites and metal-oxygen bond in tetrahedral sites respectively which would be observed in general in the spinel structures [41–44]. This observation agrees with the results of XRD analysis. The broad absorption band in the range 3435–3444 cm^{-1} can be attributed to the characteristic of absorbed water or hy-

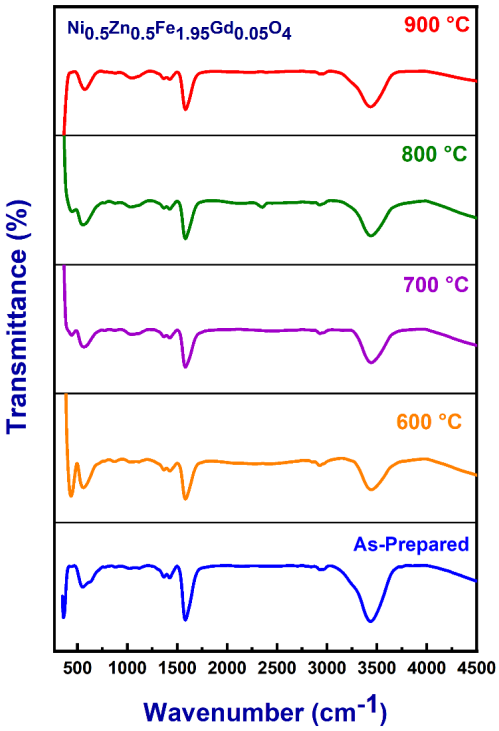

Figure 5. FTIR spectra of $Ni_{0.5}Zn_{0.5}Gd_{0.05}Fe_{1.95}O_4$ ferrite nanoparticles (as-prepared and calcinated at 600, 700, 800 & 900°C).

droxyl group in the alcohol. The absorption band in the range 2926–2933 cm^{-1} can be assigned to the formation of CH_3–CH_3–, CH_3–NH_2–, CH_3–O– bonds when the polymerization takes place with metal nitrate, citric acid, and ethylene glycol. The absorption band in the range 1021–1047 cm^{-1} is ascribed to the C–C–O structure from ethylene glycol in the polymerization process.

Table 2. Characteristic wavenumbers of $Ni_{0.5}Zn_{0.5}Gd_{0.05}Fe_{1.95}O_4$ ferrite nanoparticles (as-prepared and calcinated at 600, 700, 800 & 900°C)

Calcination temperature (°C)	ν_1 (cm^{-1})	ν_2 (cm^{-1})	ν_3 (cm^{-1})	ν_4 (cm^{-1})	ν_5 (cm^{-1})	ν_6 (cm^{-1})
As-prepared	360.62	553.47	1021.12	1581.34	2932.23	3435.56
600	435.83	560.22	1028.83	1581.34	2926.45	3443.27
700	440.65	565.04	1040.41	1568.81	2929.34	3442.31
800	447.40	555.40	1033.66	1581.34	2927.41	3440.39
900	428.11	574.68	1046.19	1582.31	2932.23	3435.36

3.4 Elastic properties

The longitudinal and shear wave velocities (v_l and v_s) of all the samples are furnished in Table 3. Both the velocities were found increased continuously with the calcination temperature as shown in Figure 6. With the support of velocity values, Poisson's ratios (σ) of all the samples were calculated by the well-known relation [47] and the calculated values were furnished in Table 3. Further the Poisson's ratio was found in the range 0.1649–0.1905. The longitudinal velocity was found increased gradually from 4250 m/s to 4338 m/s and the shear velocity was found increased gradually from 2628 m/s to 2748 m/s, whereas Poison's ratio was decreased from 0.1905 to 0.1649 with the increment of calcination temperature. As the porosity percentage was decreased from 20 to 13 with calcination temperature, the longitudinal and shear velocities increased gradually. The similar behavior was observed in earlier reports of some other CMR mate-

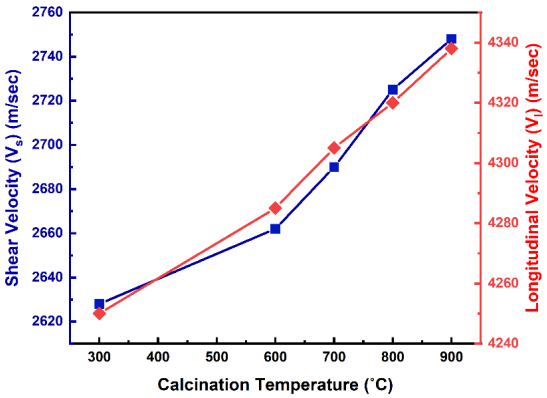

Figure 6. Variation of longitudinal and shear velocities in $Ni_{0.5}Zn_{0.5}Gd_{0.05}Fe_{1.95}O_4$ ferrite nanoparticles (as-prepared and calcinated at 600, 700, 800 & 900°C).

Table 3. Bulk & X-ray densities, porosity percentage, ultrasonic velocities and Poison's ratio of $Ni_{0.5}Zn_{0.5}Gd_{0.05}Fe_{1.95}O_4$ ferrite nanoparticles (as-prepared and calcinated at 600, 700, 800 & 900°C)

Calcination temperature (°C)	Bulk density ρ_b	X-ray density ρ_x	Porosity (%)	Longitudinal velocity v_l (m/s)	Shear velocity v_s (m/s)	Poison's ratio σ
As-prepared	3278	4097	20	4250	2628	0.1905
600	3368	4107	18	4285	2662	0.1857
700	3420	4120	17	4305	2690	0.1797
800	3510	4129	15	4320	2725	0.1696
900	3602	4140	13	4338	2748	0.1649

Table 4. Elastic moduli of $Ni_{0.5}Zn_{0.5}Gd_{0.05}Fe_{1.95}O_4$ ferrite nanoparticles (as-prepared and calcinated at 600, 700, 800 & 900°C) before and after porosity correction

Calcination temperature (°C)	Before porosity correction		After porosity correction	
	E (GPa)	G (GPa)	E_0 (GPa)	G_0 (GPa)
As-prepared	53.90	22.64	89.78	37.83
600	56.60	23.87	88.37	37.42
700	58.40	24.75	88.40	37.66
800	60.96	26.06	86.97	37.43
900	63.63	27.20	85.88	36.94

rials [45] and manganites [46]. The behavior of Young's modulus (E), rigidity modulus (G) were quite similar to longitudinal and shear velocities. The elastic moduli were also measured using the well-known methods [47] and the values are furnished in Table 4. The Young modulus and rigidity modulus values of all the samples were found to increase with the increase of calcination temperature whereas the similar behavior was detected earlier in some other CMR materials, but it was found with the variation of composition [45, 46]. It was clearly understood that the elastic properties of magnetic ceramics can also be tailored by varying the composition as well calcination temperature.

3.5 Porosity correction

The elastic properties of any material depend on the density and the porosity percentage of the testing samples [47, 48]. As the samples of the present investigation were prepared by the well-known sol-gel auto-combustion method, they exhibit ceramic nature with porosity. Hence, it was become important to measure the percentage of porosity in these materials. The percentage porosity was calculated from bulk and X-ray densities of the samples and the measured percentage porosity are presented in Table 3. The percentage porosity of all the samples was found in the range of 13–20%. As all the samples under the study were found to be porous, the measured elastic moduli would definitely be lesser than those of non-porous elastic moduli. Moreover, these values do not have any significance unless they would be corrected to zero porosity [45–47]. To calculate zero porosity corrected elastic moduli, Hasselman and Fulrath model was used [49]. This model proposed on the assumption that the samples prepared by solid state reaction method can mainly possess spherical type of pores. According to this model [49], Young's and shear wave moduli can be specified by

$$E_0 = \frac{E}{1-\alpha_E P}, \quad \text{where} \quad \alpha_E = \frac{3(9+5\sigma)(1-\sigma)}{2(7-5\sigma)}, \tag{1}$$

$$G_0 = \frac{G}{1-\alpha_G P}, \quad \text{where} \quad \alpha_G = \frac{15(1-\sigma)}{(7-5\sigma)}, \tag{2}$$

where E_0 and G_0 are the Young and Rigidity moduli of non-porous matrix respectively, whereas E and G are the experimental measured values of Young's and rigidity moduli, respectively, and P is percentage porosity of the material. By means of equations (1) and (2), porosity corrections were completed for the experimental elastic moduli and the zero porous elastic moduli were presented in Table 4. It was observed that the value of corrected zero porous Young's modulus was found to decrease continuously with the increase of calcination temperature. Similar behavior was found with doping concentration in earlier reports in the case of some manganite-based materials [49, 50].

4 Conclusions

1. The spinel ferrite of composition $Ni_{0.5}Zn_{0.5}Gd_{0.05}Fe_{1.95}O_4$ was prepared by sol-gel method successfully.
2. The X-ray diffraction patterns confirm the formation of cubic spinel structure in single phase and Fd3m space group without any impurity peaks.
3. The lattice parameter was found maximum (8.389 Å) for as-prepared sample and it was found decreased from 8.382 to 8.360 Å with the increment of calcination temperature from 600 to 900°C.
4. The crystallite size was found 17.61 nm for as-prepared sample whereas the crystallite size was increased from 11.75 nm to 18.13 nm with the increment of calcination temperature from 600 to 900°C.
5. The average grain size was found 100.2 nm for as-prepared sample and it was found increased to 152.3 nm with the calcination temperature.
6. The bulk density and X-ray density were increased with the calcination temperature whereas porosity percentage was decreased.
7. The FTIR transmission spectra showed six absorption peaks in all the samples. The first two absorption bands were found in the ranges 360–448 cm^{-1} and 553–575 cm^{-1} which attributes the presence of spinel structure.
8. The Young modulus and rigid modulus values were found to increase with the increasing the calcination temperature whereas zero porous moduli were found to decreases with increasing calcination temperature.

Acknowledgements

The authors expressed their thankfulness to the Registrar, JNTU Hyderabad, the author SDB expressed her gratitude to the Principal, Government Degree College Zaheerabad and the author MAS expressed his gratitude to the Principal, SRR Government Arts & Science College, Karimnagar for their encouragement and support in carrying out this research work.

References

[1] Y. Zhang, Z. Yang, D. Yin, Y. Liu, C. Fei, R. Xiong, J. Shi, G. Yan (2010) Composition and magnetic properties of cobalt ferrite nano-particles prepared by the co-precipitation method. *J. Magn. Magn. Mater.* **322** 3470-3475.

[2] M. Gharibshahian, O. Mirzaee, M.S. Nourbakhsh (2017) Evaluation of superparamagnetic and biocompatible properties of mesoporous silica coated cobalt ferrite nanoparticles synthesized via microwave modified Pechini method. *J. Magn. Magn. Mater.* **425** 48-56.

[3] B. Rabi, A. Essoumhi, M. Sajieddine, J.M. Greneche, E.K. Hlil, A. Razouk, M.A. Valente (2020) Structural, magnetic and magnetocaloric study of $Ni_{0.5}Zn_{0.5}Fe_2O_4$ spinel. *Appl. Phys. A* **126** 174.

[4] A.C. Gandhi, P.M. Reddy, T.-S. Chan, Y.-P. Ho, S.Y. Wu (2015) Memory effect in weakly-interacting Fe_3O_4 nanoparticles. *RSC Adv.* **5** 84782-84789.

[5] N. Guijarro, P. Bornoz, M. Prévot, X. Yu, X. Zhu, M. Johnson, X. Jeanbourquin, F. Le Formal, K. Sivula (2018) Evaluating spinel ferrites MFe_2O_4 (M = Cu, Mg, Zn) as photoanodes for solar water oxidation: prospects and limitations. *Sustainable Energy Fuels* **2** 103-117.

[6] A.M. Popov, T.A. Labutin, A.E. Goldt, O.V. Usovich, S.E. Bozhenko, N.B. Zorov (2014) Determination of lithium in lithium-ionic conductors by laser-enhanced ionization spectrometry with laser ablation. *J. Anal. At. Spectrom.* **29** 176-184.

[7] M. Colombo, S. Carregal-Romero, M.F. Casula, L. Gutiérrez, M.P. Morales, I.B. Böhm, J.T. Heverhagen, D. Prosperi, W.J. Parak (2012) Biological applications of magnetic nanoparticles *Chem. Soc. Rev.* **41** 4306.

[8] A.E. Reddy, T. Anitha, C.V.V. Muralee Gopi, S.S. Rao, B. Naresh, H.-J. Kim (2018) Construction of novel nanocomposite $ZnO@CoFe_2O_4$ microspheres grown on nickel foam for high performance electrochemical supercapacitors. *Anal. Methods* **10** 223-229.

[9] J. Xie, K. Chen, H.-Y. Lee, C. Xu, A.R. Hsu, S. Peng, X. Chen, S. Sun (2008) Ultrasmall c(RGDyK)-Coated Fe_3O_4 Nanoparticles and Their Specific Targeting to Integrin $\alpha_v\beta_3$-Rich Tumor Cells. *J. Am. Chem. Soc.* **130** 7542-7543.

[10] E. Céspedes, J.M. Byrne, N. Farrow, S. Moise, V.S. Coker, M. Bencsik, J.R. Lloyd, N.D. Telling (2014) Bacterially synthesized ferrite nanoparticles for magnetic hyperthermia applications. *Nanoscale* **6** 12958-12970.

[11] Z. Beji, L.S. Smiri, N. Yaacoub, J.-M. Grenèche, N. Menguy, S. Ammar, F. Fiévet (2010) Annealing Effect on the Magnetic Properties of Polyol-made Ni-Zn Ferrite Nanoparticles. *Chem. Mater.* **22** 1350-1366.

[12] D. Bouokkeze, J. Massoudi, W. Hzez, M. Smari, A. Bougoffa, K. Khirouni, E. Dhahri, L. Bessais (2019) Investigation of the structural, optical, elastic and electrical properties of spinel $LiZn_2Fe_3O_8$ nanoparticles annealed at two distinct temperatures. *RSC Adv.* **9** 40940-40955.

[13] K.B. Modi, S.J. Shah, N.B. Pujara, T.K. Pathak, N.H. Vasoya, I.G. Jhala (2013) Infrared spectral evolution, elastic, optical and thermodynamic properties study on mechanically milled $Ni_{0.5}Zn_{0.5}Fe_2O_4$ spinel ferrite. *J. Mol. Struct.* **1049** 250-262.

[14] G. Datt, M. Sen Bishwas, M. Manivel Raja, A.C. Abhyankar (2016) Observation of magnetic anomalies in one-step solvothermally synthesized nickel–cobalt ferrite nanoparticles. *Nanoscale* **8** 5200-5213.

[15] C.J. Brinker, G.W. Scherer (1990) "*Sol–Gel Science*". Academic Press, New York.

[16] M. Tan, Y. Köseoğlu, F. Alan,and E. Şentürk (2011) Overlapping large polaron tunneling conductivity and giant dielectric constant in $Ni_{0.5}Zn_{0.5}Fe_{1.5}Cr_{0.5}O_4$ nanoparticles (NPs). *J. Alloys Compd.* **509** 9399-9405.

[17] S.K. Pradhan, S. Bid, M. Gateshki, V. Petkov (2005) Microstructure characterization and cation distribution of nanocrystalline magnesium ferrite prepared by ball milling. *Mater. Chem. Phys.* **93** 224-230.

[18] P. Dolcet, K. Kirchberg, A. Antonello, C. Suchomski, R. Marschall, S. Diodati, R. Muñoz-Espí, K. Landfester, S. Gross (2019) Exploring wet chemistry approaches to $ZnFe_2O_4$ spinel ferrite nanoparticles with different inversion degrees: a comparative study. *Inorg. Chem. Front.* **6** 1527-1534.

[19] S. Atiq, M. Majeed, A. Ahmad, S.K. Abbas, M. Saleem, S. Riaz, S. Naseem (2017) Synthesis and investigation of structural, morphological, magnetic, dielectric and impedance spectroscopic characteristics of Ni-Zn ferrite nanoparticles. *Ceram. Int.* **43** 2486-2494.

[20] K. Vijaya Kumar, D. Ravinder (2002) Electrical conductivity of Ni–Zn–Gd ferrites. *Mater. Lett.* **52** 166-168.

[21] D. Ravinder, K. Vijaya Kumar, P. Balaya (2001) High-frequency dielectric behavior of gadolinium substituted Ni–Zn ferrites. *Mater. Lett.* **48** 210-214.

[22] L.-Z. Li, X.-X. Zhong, R. Wang, X.-Q. Tu, L. He, R.-D. Guo, Z.-Y. Xu (2017) Structural, magnetic and electrical properties in Al-substituted NiZnCo ferrite prepared via the sol–gel auto-combustion method for LTCC technology. *RSC Adv.* **7** 39198-39203.

[23] R. Lahouli, J. Massoudi, M. Smari, H. Rahmouni, K. Khirouni, E. Dhahri, L. Bessais (2019) Investigation of annealing effects on the physical properties of $Ni_{0.6}Zn_{0.4}Fe_{1.5}Al_{0.5}O_4$ ferrite. *RSC Adv.* **9** 19949-19964.

[24] K. Rama Krishna, K. Vijaya Kumar, D. Ravinder (2012) Structural and Electrical Conductivity Studies in Nickel-Zinc Ferrite. *Advances in Materials Physics and Chemistry* **2** 185-191.

[25] L.J. Berchmans, R.K. Selvan, C.O. Augustin (2004) Evaluation of Mg2+-Substituted NiFe2O4 as a Green Anode Material. *Mater. Lett.* **58** 1928-1933.

[26] Z. Yue, J. Zhou, L. Li, X. Wang, Z. Gui (2001) Effect of Copper on the Electromagnetic Properties of Mg-Zn-Cu Ferrites Prepared by Sol-Gel Auto-Combustion Method *Mater. Sci. Eng. B* **86** 64-69.

[27] A. Kusuma, E. Sagar, G. Reddy, K. Kumar (2021) Structural and Elastic Behavior of Chromium Doped $Pr_{0.5}Sr_{0.5}MnO_3$ System. *Advances in Nanoparticles* **10** 26-35.

[28] S.E. Shirsath, S.S. Jadhav, B.G. Toksha, S.M. Patange, K.M. Jadhav (2011) Influence of $Ce4^+$ ions on the structural and magnetic properties of $NiFe_2O_4$. *J. Appl. Phys.* **110** 013914.

[29] G. Dixit, J. Pal Singh, R.C. Srivastava, H.M. Agrawal (2012) Magnetic resonance study of Ce and Gd doped $NiFe_2O_4$ nano particles. *J. Magn. Magn. Mater.* **324** 479-483.

[30] Z.K. Heiba, N.G. Imam, M. Bakr Mohamed (2015) Temperature dependent cation distribution correlated with optical and magnetic properties of nanocrystalline $NiFe_{1.8}Gd_{0.2}O_4$. *J. Mol. Struct*. **1095** 61-68.

[31] K. Ugendar, S. Samanta, S. Rayaprol, V. Siruguri, G. Markandeyulu, B.R.K. Nanda (2017) Effect of frustrated exchange interactions and spin-half-impurity on the electronic structure of strongly correlated $NiFe_2O_4$. *Phys. Rev. B* **96** 035138.

[32] R.S. Yadav, J. Havlica, J. Masilko, L. Kalina, J. Wasserbauer, M. Hajduchová, V. Enev, I. Kurřitka, Z. Kožáková (2016). Impact of Nd3+ in CoFe2O4 spinel ferrite nanoparticles on cation distribution, structural and magnetic properties. *J. Magn. Magn. Mater.* **399** 109-117.

[33] V. Chaudhari, S.E. Shirsath, M.L. Mane, R.H. Kadam, S.B. Shelke, D.R. Mane (2013) Crystallographic, magnetic and electrical properties of Ni0.5Cu0.25Zn0.25LaxFe2−xO4 nanoparticles fabricated by sol-gel method. *J. Alloys Compd*. **549** 213-220.

[34] H.M.T. Farid, I. Ahmad, K.A. Bhatti, I. Ali, S.M. Ramay, A. Mahmood (2017) The effect of praseodymium on Cobalt-Zinc spinel ferrites. *Ceram. Int.* **43** 7253-7260.

[35] M.T. Farid, I. Ahmad, M. Kanwal, G. Murtaza, I. Ali, S.A. Khan (2017) The role of praseodymium substituted ions on electrical and magnetic properties of Mg spinel ferrites. *J. Magn. Magn. Mater.* **428** 136-143.

[36] S. Balaji, R. Kalai Selvan, L. John Berchmans, S. Angappan, K. Subramanian, C.O. Augustin (2005) Combustion synthesis and characterization of Sn^{4+} substituted nanocrystalline $NiFe_2O_4$. *Mater. Sci. Eng. B* **119** 119-124.

[37] H. Yao, X. Ning, H. Zhao, A. Hao, M. Ismail (2021) Effect of Gd-Doping on Structural, Optical, and Magnetic Properties of NiFe2O4 As-prepared Thin Films via Facile Sol-Gel Approach. *ACS Omega* **6** 6305-6311.

[38] Y.B. Kannan, R. Saravanan, N. Srinivasan, I. Ismail (2017) Sintering effect on structural, magnetic and optical properties of $Ni_{0.5}Zn_{0.5}Fe_2O_4$ ferrite nano particles. *J. Magn. Magn. Mater.* **423** 217-225.

[39] D. Venkatesh, K.V. Ramesh, C.V.S.S. Sastry (2017) Effect of sintering temperature on micro structural and impedance spectroscopic properties of $Ni_{0.5}Zn_{0.5}Fe_2O_4$ nano ferrite. *AIP Conference Proceedings* **1859** 020035.

[40] I. Ismail, M. Hashim, I.R. Ibrahim, R. Nazlan, F.M. Idris, S.E. Shafie, M. Mana, G. Bahmanrokh, N.H. Abdullah, W.W. Rahman (2013) Crystallinity and magnetic properties dependence on sintering temperature and soaking time of mechanically alloyed nanometer-grain $Ni_{0.5}Zn_{0.5}Fe_2O_4$. *J. Magn. Magn. Mater.* **333** 100-107.

[41] A.K. Zak, W.H.A. Majid, M. Darroudi, R. Yousefi (2011) Synthesis and characterization of ZnO nanoparticles prepared in gelatin media. *Mater. Lett.* **65** 70-73.

[42] G. Xiong, U. Pal, J. Garcia Serrano (2007) Correlations among size, defects, and photoluminescence in ZnO nanoparticles. *J. Appl. Phys.* **101** 024317.

[43] D. Rajesh, B. Vara Lakshmi, C.S. Sunandana (2012) Two-step synthesis and characterization of ZnO nanoparticles. *Physica B* **407** 4537-4539.

[44] I. Khan, S. Khan, R. Nongjai, H. Ahmed, W. Khan (2013) Structural and optical properties of gel-combustion synthesized Zr doped ZnO nanoparticles. *Opt. Mater.* **35** 1189-1193.

[45] G. Lalitha, P. Venugopal Reddy (2009) Ultrasonic Velocity Studies in the Vicinity of TC of Bismuth Doped Manganites. *J. Phys. Condens. Matter* **21** Article ID: 056003; https://doi.org/10.1088/0953-8984/21/5/056003.

[46] G. Lalitha, D. Das, D. Bahadur, P. Venugopal Reddy (2008) Elastic Behavior of La0.67Ca0.33MnO3:ZrO2 Composites. *J. Alloys Compd.* **464** 6-8. https://doi.org/10.1016/j.jallcom.2007.09.097.

[47] J.J.U. Buch, G. Lalitha, T.K. Pathak, N.H. Vasoya, V.K. Lakhani, P.V. Reddy, R. Kumar, K.B. Modi (2008) Structural and Elastic Properties of Ca-Substituted LaMnO3 at 300K. *J. Phys. D: Appl. Phys.* **41** Article ID: 025406.

[48] Antaz Ali, M.S.I. Sarker, Minhajul Islam, M.K.R. Khan, F.A. Khan, M.N.I. Khan, M.M. Rahman (2021) *Results Phys.* **25** 104251.

[49] O.L. Anderson (1965) 2-Determination and Some Uses of Isotropic Elastic Constants of Polycrystalline Aggregates Using Single-Crystal Data. In: Mason, W.P., Ed., "*Physical Acoustics*", Vol. IIIB, Academic Press, New York, p. 43. https://doi.org/10.1016/B978-0-12-395669-9.50009-6.

[50] W.A. Wooster (1953) Physical Properties and Atomic Arrangements in Crystals. *Rep. Prog. Phys.* **16** 62-82. https://doi.org/10.1088/0034-4885/16/1/302.